New Wide Band Gap Donor for Efficient Fullerene-Free All-Small-Molecule Organic Solar Cells

Liyan Yang,[†,‡] Shaoqing Zhang,[†,§] Chang He,*[,†,‡] Jianqi Zhang,*[,‡,∥] Huifeng Yao,[†,‡] Yang Yang,[∥] Yun Zhang,[†,‡] Wenchao Zhao,[†,‡] and Jianhui Hou*[,†,‡]

[†]Beijing National Laboratory for Molecular Sciences, State Key Laboratory of Polymer Physics and Chemistry, Institute of Chemistry, Chinese Academy of Sciences, Beijing 100190, China

[‡]University of Chinese Academy of Sciences, Beijing 100049, China

[§]School of Chemistry and Biology Engineering, University of Science and Technology Beijing, Beijing 100083, China

[∥]Key Laboratory of Nanosystem and Hierarchical Fabrication, National Center for Nanoscience and Technology, Beijing 100190, China

S *Supporting Information*

ABSTRACT: A new organic small molecule, DRTB-T, that incorporates a two-dimensional trialkylthienyl-substituted benzodithiophene core building block was designed and synthesized. DRTB-T has a band gap (E_g^{opt}) of 2.0 eV with a low-lying highest occupied molecular orbital (HOMO) level of −5.51 eV. Nonfullerene small-molecule solar cells consisting of DRTB-T and a nonfullerene acceptor (IC-C6IDT-IC) were constructed, and the morphology of the active layer was fine-tuned by solvent vapor annealing (SVA). The device showed a record 9.08% power conversion efficiency (PCE) with a high open-circuit voltage (V_{oc} = 0.98 V). This is the highest PCE for a nonfullerene small-molecule organic solar cell (NFSM-OSC) reported to date. Our notable results demonstrate that the molecular design of a wide band gap (WBG) donor to create a well-matched donor−acceptor pair with a low band gap (LBG) nonfullerene small-molecule acceptor, as well as subtle morphological control, provides great potential to realize high-performance NFSM-OSCs.
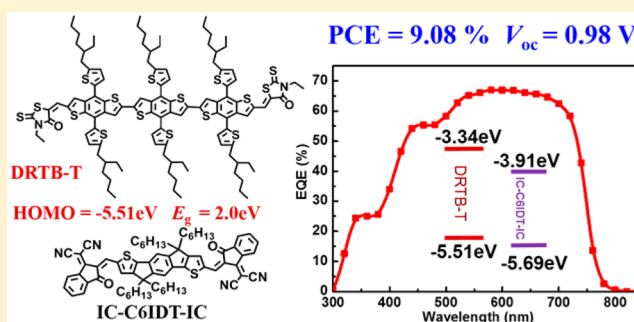
INTRODUCTION

Solution-processed bulk heterojunction organic solar cells (BHJ-OSCs) have emerged as a promising photovoltaic technology due to their potential to form large-area and flexible solar panels through low-cost solution-coating methods.[1−5] In BHJ-OSCs, the photoactive layers are made of a blend of solution-processable organic electron donors and acceptors, which can be conjugated polymers or organic small molecules. The application of fullerene derivatives as electron acceptors has greatly contributed to the advancement of the OSC field;[6−10] however, these acceptors have some inherent limitations. For example, the synthetic cost of C_{60} and C_{70}, the raw materials for making fullerene derivatives, is quite high and difficult to reduce, and the optical absorption properties of fullerenes are not strong and are hard to further enhance.[11] Therefore, many polymer and small-molecule (SM) non-fullerene acceptors have been synthesized and applied in OSCs,[12−25] and to date, over 12% power conversion efficiency (PCE) has been achieved by adopting a polymer donor and a nonfullerene SM (NFSM) acceptor in OSCs,[26] demonstrating the great potential of polymer-based fullerene-free OSCs. SM-based OSCs have attracted considerable attention because soluble organic small molecules have well-defined chemical

structures and can be prepared without batch-to-batch variations.[7,15,18] In recent years, SM-based OSCs have demonstrated PCEs comparable to those of polymer-based OSCs using fullerene acceptors,[13,27,28] but when nonfullerene acceptors were used in combination with an SM donor, the photovoltaic performance of the OSC dropped greatly.[29−36] As of now, the PCE of the state-of-the-art NFSM-OSC is only 7% (see Table 1).[36] Considering that NFSM-OSCs combine the advantages of both nonfullerene acceptors and SM-based OSCs, the study of NFSM-OSCs is an important topic in the field of OSCs.

However, compared to polymer-based fullerene-free OSCs and SM fullerene-based OSCs, it is even more challenging to realize high photovoltaic performance in NFSM-OSCs. First, unlike fullerenes, nonfullerene acceptors have anisotropic conjugated backbones and ultrafast charge transfer,[37−39] which can be greatly affected by the intermolecular packing of the electron donors and nonfullerene acceptors;[40−42] however, methods for modulating the intermolecular packing are currently still unclear. Second, in comparison with polymer-

Table 1. Photovoltaic Data of Efficient Nonfullerene Small-Molecule Solar Cells (PCE > 4%)

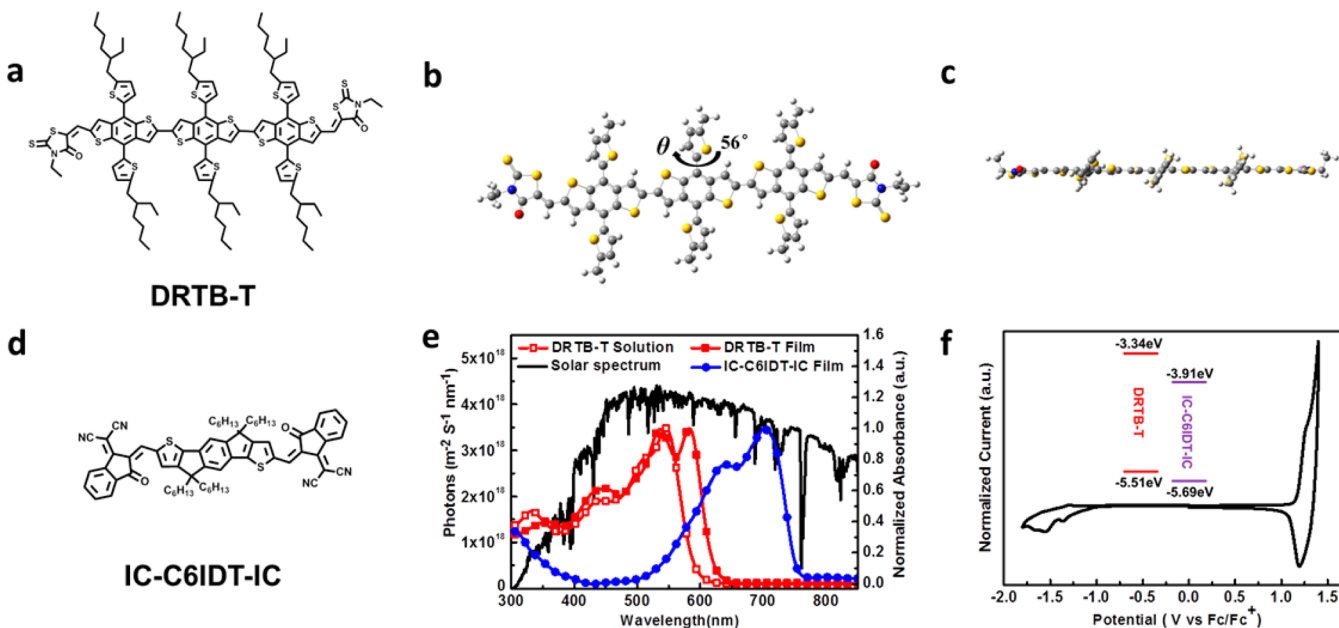| donor	acceptor	V_{oc} [V]	J_{sc} [mA/cm^2]	FF	PCE [%]	ref
BDT3TR	O-IDTBR	1.06	12.10	0.56	7.09	36
p-DTS(FBTTh$_2$)$_2$	NIDCS-MO	0.85	9.68	0.66	5.44	30
BDTS-2DPP	IEIC	0.93	9.80	0.58	5.29	33
BDT-2DPP	IEIC	0.90	8.24	0.54	4.0	33
DRTB-T	**IC-C6IDT-IC**	**0.98**	**14.25**	**0.65**	**9.08**	this work

Figure 1. (a) Molecular structure of DRTB-T. (b) Top view of the optimized geometry of DRTB-T at the B3LYP/6-31G(d, p) level. (c) Side view of the optimized geometry of DRTB-T at the B3LYP/6-31G(d, p) level. (d) Molecular structure of IC-C6IDT-IC. (e) Solution UV−vis absorption spectrum of DRTB-T and the normalized thin film absorption spectra of DRTB-T and IC-C6IDT-IC. (f) Cyclic voltammetry curve of the DRTB-T film on a glassy carbon electrode in 0.1 M Bu$_4$NPF$_6$ acetonitrile solution at a scan rate of 20 mV s^{-1} (calibrated by the Fc/Fc$^+$ redox couple).

based OSCs, the phase-separation morphology of the SM active layer and the photovoltaic properties of SM OSCs are more sensitive to the conditions during device fabrication; thus, much effort must be put into morphological control by tuning solution-processing methods.[43−46] Therefore, although the advantages of both nonfullerene acceptors and SM-based OSCs can be combined in NFSM-OSCs, the challenges for realizing high photovoltaic performance in the devices are also magnified.

The active layers in NFSM-OSCs can be optimized by designing new molecules and selecting the proper combination of donor and acceptor. In nonfullerene polymer-based OSCs (NFP-OSCs), by studying correlations among polymer structures, the intermolecular orientation of the donor and acceptor and the photovoltaic properties revealed that a face-to-face intermolecular orientation is beneficial for ultrafast charge transfer between the polymeric donors and acceptors,[42,47−49] and polymers based on alkylthienyl-substituted benzodithiophene (BDT) can afford this favorable intermolecular orientation.[48,49] For SM donors and acceptors, combining an electron-rich core unit (donor) and two electron-deficient end groups (acceptor) to form an acceptor−donor−acceptor (A−D−A)-type small molecule is an effective strategy to tune the optical absorption and molecular energy levels, by which quite a few highly efficient photovoltaic materials have been obtained.[33,50] In comparison with A−D−A donors, A−D−A acceptors, such as ITIC,[51] IT-M,[26] and IEICO,[52] possess more

red-shifted absorption spectra and lower molecular energy levels due to the strong electron-withdrawing effect of their end groups. Thus, the combination of A−D−A donors and acceptors can afford broad absorption spectra and appropriate molecular energy levels, which are two key factors for realizing the efficient harvest of sunlight and the generation of free charges.[53−55] In addition to the molecular design, the reported works also demonstrated many useful methods to modulate phase-separation morphologies in oligomer and polymer solar cells. For example, thermal annealing (TA), solvent vapor annealing (SVA), and solvent additives can be used to enhance the crystallinity of the donors and modulate the phase-separation morphology of the active layers. Overall, the achievements in fullerene-based SM OSCs (FSM-OSCs) and NFP-OSCs provide important knowledge to optimize the molecular structures and morphologies of the active layers in NFSM-OSCs.

In this work, an A−D−A small molecule, namely, DRTB-T (Figure 1a), was designed using an alkylthienyl-substituted BDT trimer as the central unit and 3-ethylrhodanines as the end-capping groups. DRTB-T has a band gap (E_g^{opt}) of 2.0 eV with a low-lying highest occupied molecular orbital (HOMO) level of −5.51 eV. NFSM-OSCs were then fabricated by employing DRTB-T as the donor and selecting another A−D−A small molecule, IC-C6IDT-IC,[56] as the acceptor. After optimizing the phase-separation morphology and crystallinity of the donor and acceptor in the active layers by SVA, a PCE of

Scheme 1. Synthetic Route of DRTB-T
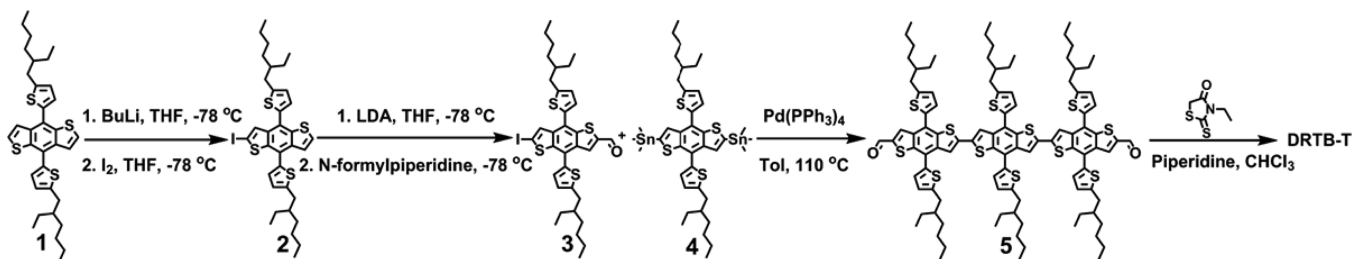
9.08% was achieved, which is the highest value for NFSM-OSCs to date.

RESULTS AND DISCUSSION

Consideration of the Molecular Design and Synthesis of DRTB-T. As most SM donors and acceptors with A−D−A structures possess strong intramolecular charge transfer (ICT) effects by which E_g^{opt} can be significantly reduced, these molecules often show low band gap (LBG) features. A−D−A SM donors and acceptors have demonstrated outstanding photovoltaic properties in OSCs.[14,28,50,57,58] However, there are some differences in their electronic properties. To facilitate light-induced ultrafast charge transfer in OSCs, end groups with stronger electron-withdrawing effects are commonly used in A−D−A SM acceptors, which ensure that both the HOMO and lowest unoccupied molecular orbital (LUMO) levels of the acceptors are lower than those of the donors, leading to lower E_g^{opt}. That is, A−D−A SM acceptors often possess lower E_g^{opt}.[33] Therefore, the combination of an LBG A−D−A acceptor and a wide band gap (WBG) A−D−A donor can provide broad optical absorption and appropriate molecular energy level arrangement and thus should be the optimal choice for fabricating efficient NFSM-OSCs. For A−D−A photovoltaic materials, the optical absorption edge of high performance donors reported in previous works is beyond 700 nm,[13,27] corresponding to E_g^{opt} < 1.77 eV, which greatly overlaps with the absorption spectra of highly efficient A−D−A acceptors.[11,16] Therefore, to significantly improve the PCE of NFSM-OSCs, it is necessary to design and synthesize new WBG A−D−A donors.

Here, we designed an A−D−A small molecule, namely, DRTB-T, shown in Figure 1a. In this molecule, a 2-ethylhexylthienyl-substituted BDT trimer is employed as the central unit, and two 3-ethylrhodanines are used as end-capping groups. The optimal geometry of DRTB-T was obtained by theoretical calculation with density functional theory (DFT) at the B3LYP/6-31G(d, p) level. As shown in Figure 1b,c (top and side views, respectively), the dihedral angle between the BDT units is 180°, meaning that DRTB-T has a linear backbone with good planarity; the dihedral angle between BDT and the thiophene side groups is approximately 56°. The HOMO and LUMO surfaces are well-delocalized along the three BDT units and are partially distributed to the thiophene side groups, although they are twisted from the BDT backbone (Figure S3). Because the optimal geometry is obtained without considering intermolecular π−π interactions, which can reduce the dihedral angle between thiophene and BDT, we can reasonably infer that the thiophene units can be well-conjugated with the backbone in the solid thin film.

DRTB-T was synthesized using the route shown in Scheme 1. Compound **2** was obtained by an iodination reaction using n-butyllithium and iodine in tetrahydrofuran (THF) at −78 °C in a yield of 74%. Compound **2** was treated with lithium diisopropylamide (LDA) at −78 °C and then reacted with N-formylpiperidine to produce compound **3** in a yield of 82%. Compound **5** was prepared in a yield of 68% through a commonly used Stille coupling reaction using compound **3** and a commercially available bis-trimethyltin BDT derivative as the starting materials. Finally, DRTB-T was obtained in a yield of 80% by a Knoevenagel reaction between compound **5** and 3-ethylrhodanine. DRTB-T was characterized by ^1H and ^{13}C nuclear magnetic resonance (NMR) spectroscopy. Thermogravimetric analysis (TGA) demonstrated that DRTB-T has excellent thermal stability (5% weight loss at 411 °C, Figure S4); the melting temperature (T_m) and recrystallization temperature (T_c) measured by differential scanning calorimetry (DSC) were 287 and 218 °C, respectively (Figure S5). DRTB-T can be easily dissolved in commonly used organic solvents, such as chloroform, tetrahydrofuran, chlorobenzene, and toluene.

UV−vis Absorption Spectra and Molecular Energy Levels of DRTB-T. As shown in Figure 1e, the dilute solution of DRTB-T in chloroform exhibits an absorption peak in the range of 300−600 nm, with a high molar extinction coefficient (ε) of 1.2×10^5 M^{-1} cm^{-1} at 545 nm. For the solid film, the absorption peak at 545 nm has almost no change, while a strong absorption shoulder peak appears at 585 nm, which is ascribed to the π−π* transition due to strong intermolecular π−π interactions in the solid state. DRTB-T shows an absorption edge at 620 nm, corresponding to an E_g^{opt} of 2.0 eV. Electrochemical measurements were used to evaluate the HOMO and LUMO levels of DRTB-T. As shown in Figure 1f, the p- and n-doping processes of DRTB-T are quasi-reversible, and according to the onset potentials of the p- and n-doping processes and the standard redox potential of ferrocene/ferrocenium (Fc/Fc⁺), the HOMO and LUMO levels of DRTB-T were estimated to be −5.51 and −3.34 eV, respectively.

Photovoltaic Properties of the NFSM-OSCs based on DRTB-T and IC-C6IDT-IC. As described above, DRTB-T has a strong absorption peak under 620 nm and a HOMO level of −5.51 eV. The absorption spectrum of DRTB-T is complementary to those of many LBG NFSM acceptors with A−D−A structures. However, only a few NFSM acceptors can be matched with DRTB-T when considering their molecular energy level arrangement because DRTB-T possesses a low-lying HOMO level. Here, as shown in Figure 1d, we selected a recently reported A−D−A SM acceptor, namely, IC-C6IDT-IC, to use with DRTB-T in NFSM-OSCs. The absorption spectrum and molecular energy levels of IC-C6IDT-IC are shown in Figures 1e,f, respectively. Clearly, the absorption spectra of DRTB-T and IC-C6IDT-IC complement each other
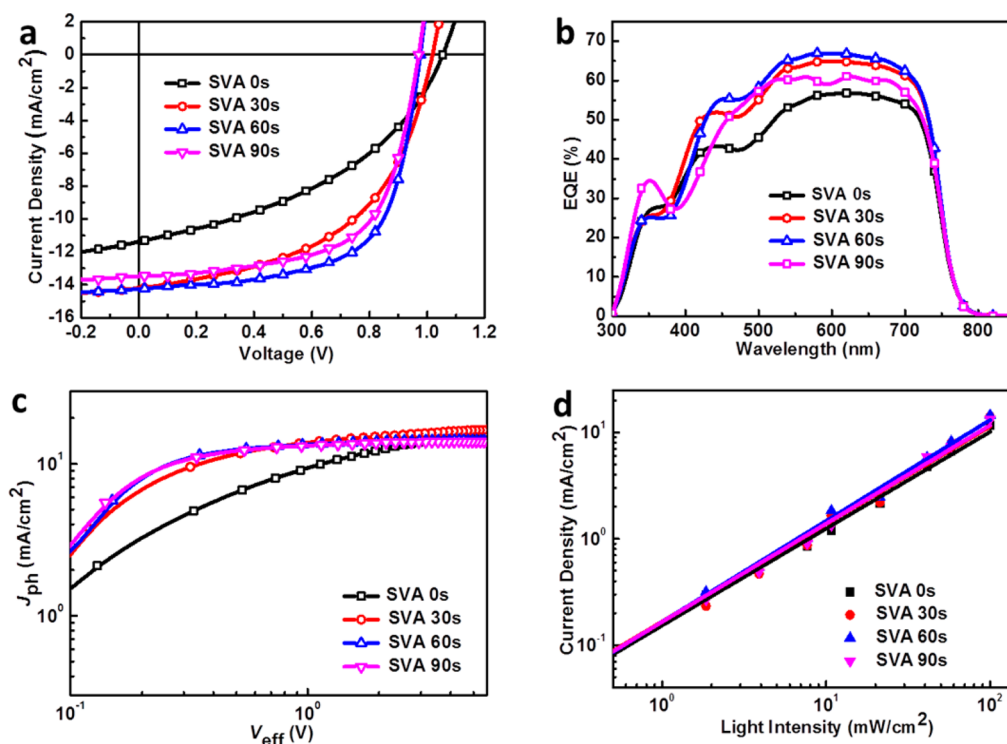
Figure 2. (a) $J-V$ curves, (b) EQE spectra, (c) $J_{ph}-V_{eff}$ curves, and (d) $J_{sc}-P$ curves of DRTB-T:IC-C6IDT-IC BHJ devices after SVA treatment for 0, 30, 60, and 90 s. The solid lines in the $J_{sc}-P$ curves are the fitted curves.

Table 2. Photovoltaic Properties of DRTB-T:IC-C6IDT-IC BHJ Devices with Different SVA Treatment Times

SVA time [s]	V_{oc} [V]	J_{sc} (J_{sc}) [mA/cm^2][a]	FF	PCE$_{max}$ [%]	PCE$_{avg}$ [%][b]	μ_h [cm^2 V^{-1} s^{-1}][c]	μ_e [cm^2 V^{-1} s^{-1}][d]
0	1.05	11.37 (11.98)	0.42	5.03	4.91 ± 0.05	5.79 × 10^{-6}	6.14 × 10^{-5}
30	1.02	14.17 (13.86)	0.52	7.47	7.44 ± 0.03	6.85 × 10^{-5}	8.70 × 10^{-5}
60	0.98	14.25 (14.23)	0.65	9.08	8.85 ± 0.08	3.46 × 10^{-4}	2.89 × 10^{-4}
90	0.97	13.49 (13.09)	0.63	8.25	8.20 ± 0.07	2.64 × 10^{-4}	1.59 × 10^{-4}

[a]Calculated by integration of the EQE curves. [b]The average values were obtained over 10 devices. [c]The hole-only devices had the structure ITO/PEDOT:PSS/DRTB-T:IC-C6IDT-IC/Au. [d]The electron-only devices had the structure ITO/ZnO/DRTB-T:IC-C6IDT-IC/Al.

well, and both the HOMO and LUMO levels of IC-C6IDT-IC are obviously lower than those of DRTB-T, which can afford a sufficient driving force for exciton dissociation.[59,60] Therefore, the combination of these two SM materials is suitable for making NFSM-OSCs.

NFSM-OSC devices were fabricated with a normal structure, i.e., ITO/MoO$_3$ (10 nm)/DRTB-T:IC-C6IDT-IC/Al (100 nm), and characterized to investigate the photovoltaic properties of the DRTB-T:IC-C6IDT-IC blend. The optimal device was obtained by varying the donor to acceptor weight ratio (D/A, w/w) in the active layer and by modulating the thickness of the active layer, and the detailed data for optimizing the device fabrication conditions are summarized in Tables S1 and S2 and Figures S6 and S7. Then, the photovoltaic performance of the device with the optimal D/A ratio (1:1.25) and thickness (ca. 80 nm) was further improved by adopting dichloromethane (DCM) as the solvent vapor source for SVA treatment. Figure 2a shows the current density−voltage (J−V) curves of the devices under 100 mW/cm^2 AM 1.5G illumination with different SVA treatment times (0, 30, 60, and 90 s), and the corresponding photovoltaic parameters are summarized in Table 2. While the as-cast device exhibited a PCE of 5.03%, it could be distinctly enhanced to 7.47% by 30 s of SVA treatment; after being treated for 60 s, the PCE was improved

to 9.08%, with an open-circuit voltage (V_{oc}) of 0.98 V, short circuit current density (J_{sc}) of 14.25 mA/cm^2, and fill factor (FF) of 0.65. A PCE of 9.08% is by far the highest value for NFSM-OSCs and a good result for all types of BHJ-OSCs. Compared to the untreated devices, the enhanced PCE of the SVA-treated devices is largely a result of the increased J_{sc} and FF, and when the devices were subjected to SVA for up to 90 s, the values of J_{sc} and FF were slightly reduced.

The external quantum efficiency (EQE) spectra of the devices for different SVA treatment times are shown in Figure 2b. The broad and efficient EQE spectra from 300 to 780 nm suggest that both DRTB-T and IC-C6IDT-IC make beneficial contributions to the EQE. The J_{sc} values calculated from the integration of the EQE spectra agree well with the J_{sc} values from the J−V measurements with a 2−3% mismatch. For comparison, DRTB-T:PC$_{71}$BM reference devices were also fabricated (Figure S9). Due to the narrower optical absorption of the fullerene acceptor compared to that of the nonfullerene acceptor, the EQE spectral response of the PC$_{71}$BM-based solar cell was mainly between 300 and 620 nm, leading to a much lower J_{sc} than that of the nonfullerene acceptor-based device.

Then, the hole and electron mobilities (μ_h and μ_e) of the DRTB-T:IC-C6IDT-IC blend films for various SVA treatment times were measured by the space-charge-limited current
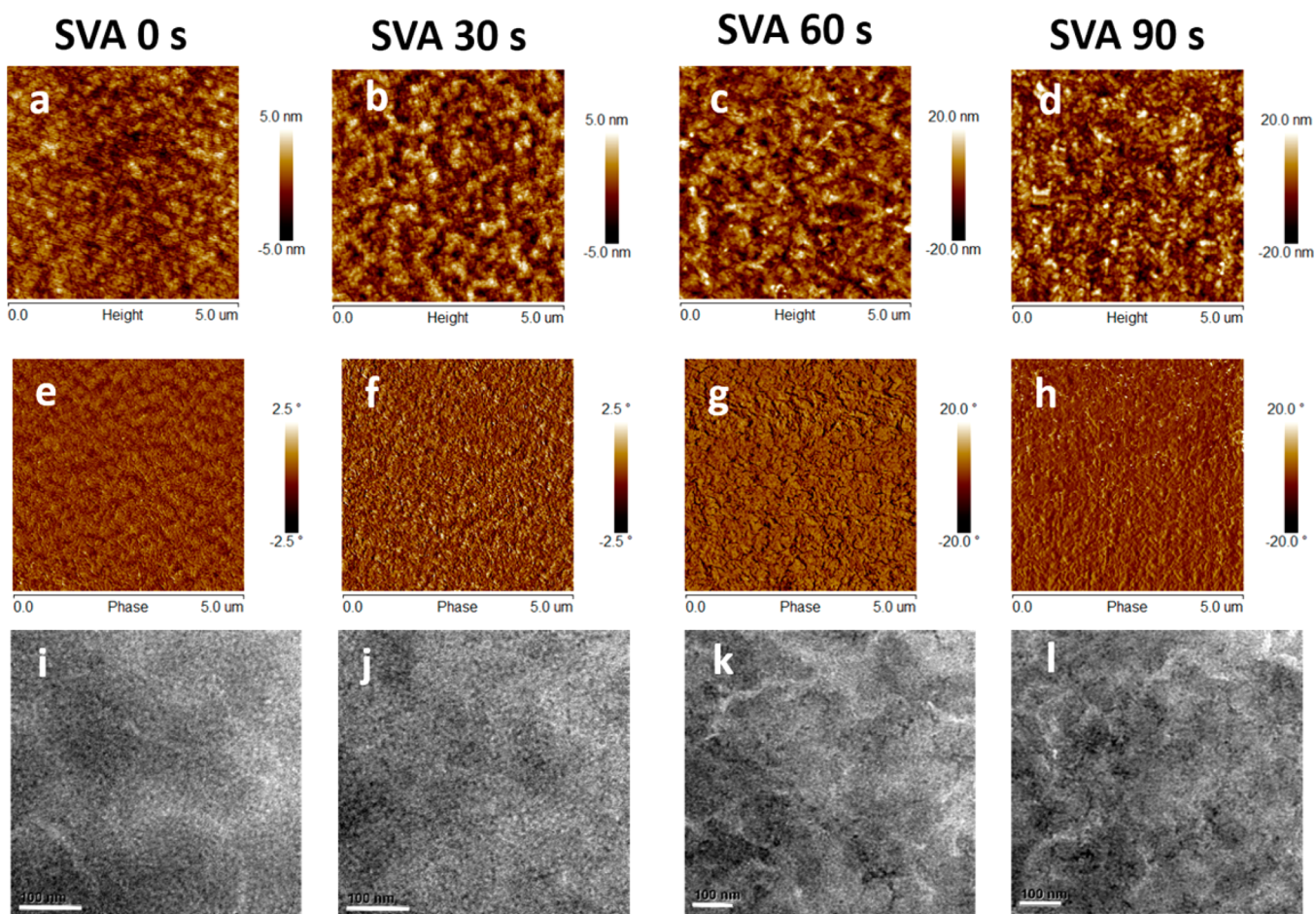
Figure 3. AFM height and phase images (5 × 5 μm) of films spin-coated from the DRTB-T:IC-C6IDT-IC blend with various SVA treatment times: (a, e) as-cast and after SVA treatment for (b, f) 30 s, (c, g) 60 s, and (d, h) 90 s. The RMS roughness values were 1.24, 1.54, 5.75, and 6.0 nm, respectively. Bright-field (BF)-TEM images of the films spin-coated from the DRTB-T:IC-C6IDT-IC blend with various SVA treatment times: (i) as-cast and after SVA treatment for (j) 30 s, (k) 60 s, and (l) 90 s. The scale bars correspond to 100 nm.

(SCLC) model.[61,62] The hole mobility was measured by adopting a hole-only device structure, ITO/PEDOT:PSS/DRTB-T:IC-C6IDT-IC/Au, and the electron mobility was measured with an electron-only device structure, ITO/ZnO/DRTB-T:IC-C6IDT-IC/Al (Figure S10). The μ_h and μ_e values of the blend films treated for different times are summarized in Table 2. For the as-cast device, μ_h is 5.79×10^{-6} cm^2 V^{-1} s^{-1}, which is approximately 1 order of magnitude lower than the electron mobility, and the asymmetric mobility of the electron and hole will induce strong charge carrier recombination and thus lead to low FF and J_{sc}. After SVA treatment, both the hole and electron mobilities of the blend films increased, and under the optimal conditions, i.e., treated by SVA for 60 s, the μ_h and μ_e values of the blend film reached 3.46×10^{-4} and 2.89×10^{-4} cm^2 V^{-1} s^{-1}, respectively, and the high and symmetric hole and electron mobilities resulted in a high J_{sc} and good FF in this device.

Recombination Mechanism by Analysis of the J−V Characteristics. To understand the recombination mechanism involved in the DRTB-T:IC-C6IDT-IC all-SM solar cells, the photocurrent density (J_{ph}) versus the effective voltage (V_{eff}) of the devices with different SVA treatment times were measured and are shown in Figure 2c. J_{ph} is defined as $J_{ph} = J_L − J_D$, where J_L and J_D are the current densities under illumination and in the dark, respectively. V_{eff} is defined as $V_{eff} = V_0 − V_a$, where V_0 is

the voltage at which $J_{ph} = 0$ and V_a is the applied voltage. The photocurrent was saturated at $V_{eff} = 2−6$ V, and the resulting exciton dissociation probability (P_{diss}, determined by the normalized J_{ph} at the saturated current density) under short-circuit conditions was determined.[62,63] In the as-cast device, only 64.9% of the photogenerated excitons dissociated, providing a rather low contribution to J_{sc}, which indicates that geminate charge recombination is a form of major loss in the as-cast device due to the low charge mobility. The P_{diss} values were calculated to be 84.5, 97.1, and 95.6% for SVA treatment times of 30, 60, and 90 s, respectively. The higher values obtained after SVA treatment support the superior performance of SVA-treated devices compared to those of devices that did not undergo SVA treatment. For devices treated with SVA for 60 s, the P_{diss} value of 97.1%, near 100%, implies that the geminate recombination loss of photogenerated excitons is negligible.[64] The light-intensity-dependent J_{sc} was also determined to identify nongeminate recombination losses in the devices fabricated under different conditions. The relationship between J_{sc} and light intensity follows the relation $J_{sc} \propto P^S$, where P is the light intensity and S is the exponential factor. As shown in Figure 2d, the data are plotted on a log−log scale, and the fitted slope (S) in the devices was calculated to be 0.91, 0.92, 0.95, and 0.93 for SVA treatment times of 0, 30, 60, and 90 s, respectively. This
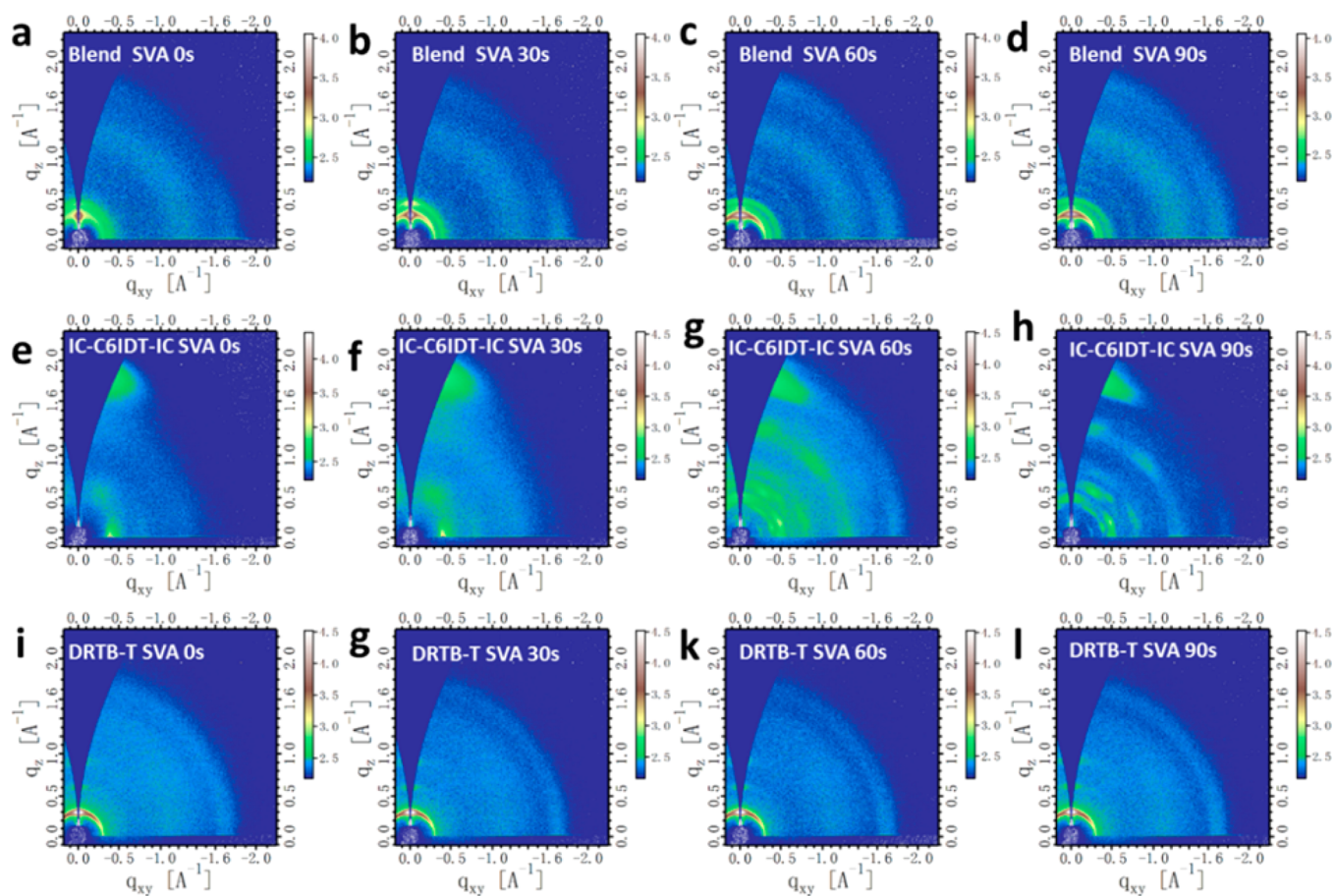
Figure 4. 2D GIWAXS patterns of neat DRTB-T, neat IC-C6IDT-IC, and blend films with different SVA treatment times.
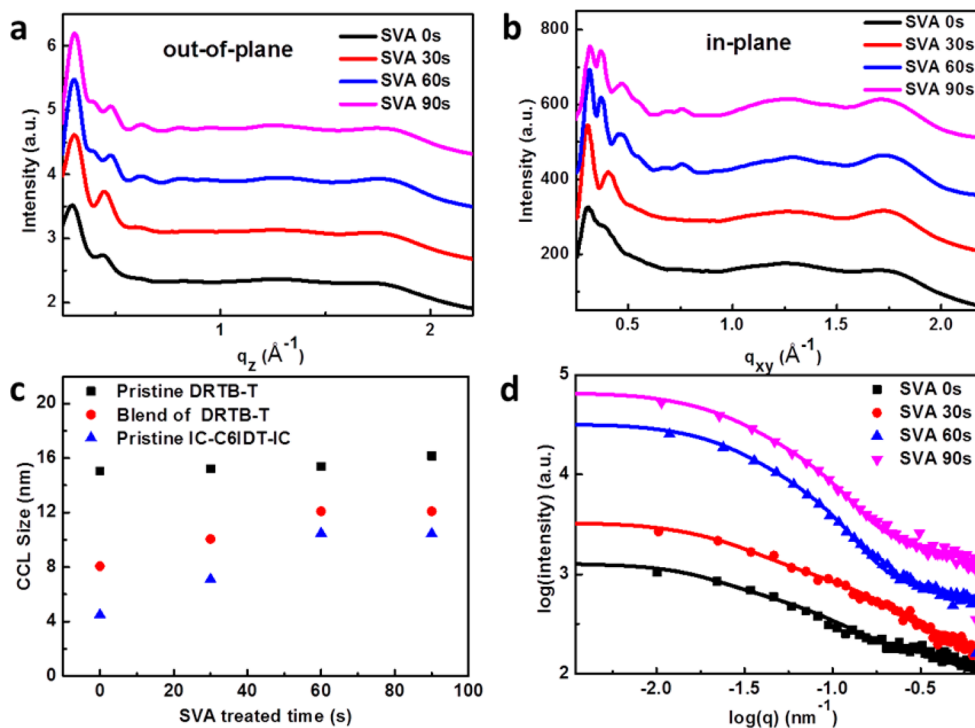

Figure 5. (a) Out-of-plane and (b) in-plane cuts of the GIWAXS patterns for the blend films with different SVA treatment times. (c) CCL of neat DRTB-T, neat IC-C6IDT-IC, and blend films with different SVA treatment times, where CCL was calculated using the Scherrer equation. (d) In-plane GISAXS profiles (symbols) and the corresponding fit (lines) with a 1D paracrystalline model under different SVA treatment times.

indicates that bimolecular recombination was minimized with SVA treatment with DCM for 60 s, which also agrees well with the remarkable increase in FF from 0.42 to 0.65 upon increasing the SVA treatment time to 60 s.

Morphological Study of the DRTB-T:IC-C6IDT-IC Blend Films. To further understand the relationship between the evolution of the active layer morphology and device performance, the surface morphology of the DRTB-T:IC-C6IDT-IC blend films with various SVA treatment times were investigated using atomic force microscopy (AFM). As shown in Figure 3a–h, the film processed without SVA treatment presents uniform and smooth features with a root-mean-square (RMS) roughness of 1.24 nm. For the SVA-treated films, apparent aggregation features are seen with increased RMS values of 1.54, 5.75, and 6.0 nm corresponding to SVA treatment times of 30, 60, and 90 s, respectively. These results suggest that SVA treatment induced the aggregation of DRTB-T and IC-C6IDT-IC in the blend films. Transmission electron microscopy (TEM) was performed to monitor the bulk morphology of the DRTB-T:IC-C6IDT-IC blend films (Figure 3i–l). The TEM images clearly show large morphological changes upon SVA treatment, which agree well with the AFM morphology observations. With increasing SVA treatment time, the tendency toward nanoscale phase separation in the blend films increased. Interestingly, fine small-domain regions and interconnected phase-separated domains were observed in the samples with SVA treatment times of 60 and 90 s, and this formation of interconnected structures in the blend films led to more efficient exciton dissociation and charge-carrier transport processes. The similar elemental composition of the donor and acceptor molecules in the blend films makes it difficult to distinguish which composition corresponds to the dark and light regions.

The following grazing-incidence wide-angle X-ray scattering (GIWAXS) measurements and analyses were performed to provide insight into the crystallinity and molecular orientation of the blend films with various SVA treatment times. Figure 4 presents the 2D GIWAXS patterns of neat DRTB-T, neat IC-C6IDT-IC, and the blend films with different SVA treatment times. The corresponding intensity profiles in the out-of-plane and in-plane directions are given in Figure 5a–b. For the as-cast IC-C6IDT-IC film, the $\pi-\pi$ stacking peak (010) represents the out-of-plane direction, while the lamellar scattering (100) peak represents the in-plane direction, indicating a typical face-on orientation.[65] The scattering intensity increased when the films were treated with SVA for 30 s. Interestingly, scattering spots are present in the 2D GIWAXS patterns of the films treated for 60 and 90 s, indicating that large crystallites were formed. The mean size of the crystallites can be obtained by calculating the crystal coherence length (CCL) using the Scherrer equation.[66] The variation in CCL with treatment time is shown in Figure 5c. It is clearly seen that CCL increases gradually from 4 to 9 nm during the first 60 s and then maintains almost the same value after 60 and 90 s of treatment. For the neat DRTB-T films, the 2D GIWAXS patterns exhibit strong lamellar (100) and (200) diffraction peaks and even (300) diffraction peaks in the out-of-plane direction, indicating a high degree of molecular ordering. However, the crystallinity does not change with SVA treatment, as evidenced by the unchanged CCL (Figure 5c). Compared with IC-C6IDT-IC, DRTB-T has a larger CCL (approximately 15 nm); however, IC-C6IDT-IC reorganizes under SVA more easily (see Figure 4). The as-cast blend film shows two broad peaks at 0.3 and 0.43 Å^{-1} in the out-of-plane

direction, which belong to the donor and acceptor, respectively. This means that the interaction between the two molecules affects crystallization. When the film was treated with SVA, the diffraction peaks became sharper, and a higher order of the peaks was present (see Figure 5). The CCLs of the donor are 8, 10, 12, and 12 nm for treatment times of 0, 30, 60, and 90 s, respectively. This means that crystallization significantly increased after SVA treatment, resulting in better charge transport and less charge recombination, as evidenced by the improved FF and hole mobility.

To address the nanoscale morphology of the active layer, grazing-incidence small-angle X-ray scattering (GISAXS) measurements were carried out. Figure 5d plots the in-plane intensity profiles with different SVA treatment times, and the 2D GISAXS patterns are given in Figure S11. Information on the lateral structures can be extracted by fitting the intensity profile with a 1D paracrystalline model.[67] Two distinct structures (small and large) were identified by proper fitting of the intensity profiles (solid lines in Figure 5d). We propose that the large domains originate from the aggregation of donor molecules due to high crystallinity, and the small domains come from the acceptor molecules. The extracted smaller domain sizes are 6.5, 8, 11.5, and 12.5 nm and the larger domain sizes are 12, 17, 22, and 29 nm for treatment with times of 0, 30, 60, and 90 s, respectively. Both domains increase with increasing SVA treatment time, which is in agreement with the AFM results, which showed increased roughness due to the formation of larger domains, as well as the observed TEM images. Consequently, the purity of the system increased, resulting in better charge transport and less recombination, which may explain the light-intensity-dependence results as well (Figure 2d). However, large domains (29 nm) would weaken the exciton separation efficiency, resulting in a reduced J_{sc} for samples treated for 90 s.

■ CONCLUSIONS

We designed and synthesized a WBG molecule, DRTB-T, with a band gap of 2.0 eV and a HOMO level of −5.51 eV. NFSM-OSCs using DRTB-T and a nonfullerene acceptor (IC-C6IDT-IC) were constructed. The morphology of the active layer was fine-tuned by SVA, which induced the desired interconnected nanoscale structure, and the corresponding device exhibited a record 9.08% PCE with a high V_{oc} of 0.98 V. This is the highest PCE for NFSM-OSCs reported to date. Our notable results demonstrate that the rational molecular design of a WBG donor, matched in a donor−acceptor pair with a LBG NFSM acceptor, along with subtle morphological control, allow for the realization of high-performance NFSM-OSCs.

■ ASSOCIATED CONTENT

ⓢ Supporting Information

The Supporting Information is available free of charge on the ACS Publications website at DOI: 10.1021/jacs.6b11612.

> Synthetic route of DRTB-T, full experimental details, ^{1}H and ^{13}C NMR spectra of DRTB-T, TGA and DSC plots of DRTB-T, molecular energy levels of DRTB-T, $J-V$, EQE curves and photovoltaic parameters of the OSCs, and 2D GISAXS patterns for the blend films (PDF)

■ AUTHOR INFORMATION

Corresponding Authors

*E-mail: hechang@iccas.ac.cn.

*E-mail: zhangjq@nanoctr.cn.
*E-mail: hjhzlz@iccas.ac.cn.

ORCID

Chang He: 0000-0002-9804-5455

Notes

The authors declare no competing financial interest.

■ REFERENCES

(1) Blom, P. W. M.; Mihailetchi, V. D.; Koster, L. J. A.; Markov, D. E. *Adv. Mater.* **2007**, *19*, 1551−1566.

(2) Brabec, C. J.; Gowrisanker, S.; Halls, J. J. M.; Laird, D.; Jia, S. J.; Williams, S. P. *Adv. Mater.* **2010**, *22*, 3839−3856.

(3) Chen, J. W.; Cao, Y. *Acc. Chem. Res.* **2009**, *42*, 1709−1718.

(4) Gunes, S.; Neugebauer, H.; Sariciftci, N. S. *Chem. Rev.* **2007**, *107*, 1324−1338.

(5) Yu, G.; Gao, J.; Hummelen, J. C.; Wudl, F.; Heeger, A. J. *Science* **1995**, *270*, 1789−1791.

(6) Dennler, G.; Scharber, M. C.; Brabec, C. J. *Adv. Mater.* **2009**, *21*, 1323−1338.

(7) Mishra, A.; Bauerle, P. *Angew. Chem., Int. Ed.* **2012**, *51*, 2020−2067.

(8) Thompson, B. C.; Frechet, J. M. J. *Angew. Chem., Int. Ed.* **2008**, *47*, 58−77.

(9) Walker, B.; Kim, C.; Nguyen, T. Q. *Chem. Mater.* **2011**, *23*, 470−482.

(10) Liu, Y. H.; Zhao, J. B.; Li, Z. K.; Mu, C.; Ma, W.; Hu, H. W.; Jiang, K.; Lin, H. R.; Ade, H.; Yan, H. *Nat. Commun.* **2014**, *5*, 5293.

(11) Lin, Y. Z.; Li, Y. F.; Zhan, X. W. *Chem. Soc. Rev.* **2012**, *41*, 4245−4272.

(12) Facchetti, A. *Mater. Today* **2013**, *16*, 123−132.

(13) Kan, B.; Li, M. M.; Zhang, Q.; Liu, F.; Wan, X. J.; Wang, Y. C.; Ni, W.; Long, G. K.; Yang, X.; Feng, H. R.; Zuo, Y.; Zhang, M. T.; Huang, F.; Cao, Y.; Russell, T. P.; Chen, Y. S. *J. Am. Chem. Soc.* **2015**, *137*, 3886−3893.

(14) Li, M. M.; Ni, W.; Wan, X. J.; Zhang, Q.; Kan, B.; Chen, Y. S. *J. Mater. Chem. A* **2015**, *3*, 4765−4776.

(15) Lin, Y. Z.; Zhan, X. W. *Mater. Horiz.* **2014**, *1*, 470−488.

(16) McAfee, S. M.; Topple, J. M.; Hill, I. G.; Welch, G. C. *J. Mater. Chem. A* **2015**, *3*, 16393−16408.

(17) Nielsen, C. B.; Holliday, S.; Chen, H. Y.; Cryer, S. J.; McCulloch, I. *Acc. Chem. Res.* **2015**, *48*, 2803−2812.

(18) Zhan, C. L.; Zhang, X. L.; Yao, J. N. *RSC Adv.* **2015**, *5*, 93002−93026.

(19) Zhang, Q.; Kan, B.; Liu, F.; Long, G. K.; Wan, X. J.; Chen, X. Q.; Zuo, Y.; Ni, W.; Zhang, H. J.; Li, M. M.; Hu, Z. C.; Huang, F.; Cao, Y.; Liang, Z. Q.; Zhang, M. T.; Russell, T. P.; Chen, Y. S. *Nat. Photonics* **2014**, *9*, 35−41.

(20) Zhao, J. B.; Li, Y. K.; Lin, H. R.; Liu, Y. H.; Jiang, K.; Mu, C.; Ma, T. X.; Lai, J. Y. L.; Hu, H. W.; Yu, D. M.; Yan, H. *Energy Environ. Sci.* **2015**, *8*, 520−525.

(21) Lin, H. R.; Chen, S. S.; Li, Z. K.; Lai, J. Y. L.; Yang, G. F.; McAfee, T.; Jiang, K.; Li, Y. K.; Liu, Y. H.; Hu, H. W.; Zhao, J. B.; Ma, W.; Ade, H.; Yan, H. *Adv. Mater.* **2015**, *27*, 7299−7304.

(22) Lin, H. R.; Chen, S. S.; Hu, H. W.; Zhang, L.; Ma, T. X.; Lai, J. Y. L.; Li, Z. K.; Qin, A. J.; Huang, X. H.; Tang, B. Z.; Yan, H. *Adv. Mater.* **2016**, *28*, 8546−8551.

(23) Li, Z.; Jiang, K.; Yang, G. F.; Lai, J. Y. L.; Ma, T. X.; Zhao, J. B.; Ma, W.; Yan, H. *Nat. Commun.* **2016**, *7*, 13094.

(24) Holliday, S.; Ashraf, R. S.; Nielsen, C. B.; Kirkus, M.; Rohr, J. A.; Tan, C. H.; Collado-Fregoso, E.; Knall, A. C.; Durrant, J. R.; Nelson, J.; McCulloch, I. *J. Am. Chem. Soc.* **2015**, *137*, 898−904.

(25) Holliday, S.; Ashraf, R. S.; Wadsworth, A.; Baran, D.; Yousaf, S. A.; Nielsen, C. B.; Tan, C. H.; Dimitrov, S. D.; Shang, Z. R.; Gasparini, N.; Alamoudi, M.; Laquai, F.; Brabec, C. J.; Salleo, A.; Durrant, J. R.; McCulloch, I. *Nat. Commun.* **2016**, *7*, 11585.

(26) Li, S.; Ye, L.; Zhao, W.; Zhang, S.; Mukherjee, S.; Ade, H.; Hou, J. *Adv. Mater.* **2016**, *28*, 9423−9428.

(27) Wang, J. L.; Liu, K. K.; Yan, J.; Wu, Z.; Liu, F.; Xiao, F.; Chang, Z. F.; Wu, H. B.; Cao, Y.; Russell, T. P. *J. Am. Chem. Soc.* **2016**, *138*, 7687−7697.

(28) Deng, D.; Zhang, Y. J.; Zhang, J. Q.; Wang, Z. Y.; Zhu, L. Y.; Fang, J.; Xia, B.; Wang, Z.; Lu, K.; Ma, W.; Wei, Z. X. *Nat. Commun.* **2016**, *7*, 13740.

(29) Feng, G. T.; Xu, Y. H.; Zhang, J. Q.; Wang, Z. W.; Zhou, Y.; Li, Y. F.; Wei, Z. X.; Li, C.; Li, W. W. *J. Mater. Chem. A* **2016**, *4*, 6056−6063.

(30) Kwon, O. K.; Park, J. H.; Kim, D. W.; Park, S. K.; Park, S. Y. *Adv. Mater.* **2015**, *27*, 1951−1956.

(31) Kwon, O. K.; Park, J. H.; Park, S. Y. *Org. Electron.* **2016**, *30*, 105−111.

(32) Lin, Y. Z.; Wang, J. Y.; Dai, S. X.; Li, Y. F.; Zhu, D. B.; Zhan, X. W. *Adv. Energy Mater.* **2014**, *4*, 1400420.

(33) Lin, Y. Z.; Zhan, X. W. *Acc. Chem. Res.* **2016**, *49*, 175−183.

(34) Ni, W.; Li, M. M.; Kan, B.; Liu, F.; Wan, X. J.; Zhang, Q.; Zhang, H. T.; Russell, T. P.; Chen, Y. S. *Chem. Commun.* **2016**, *52*, 465−468.

(35) Sharenko, A.; Proctor, C. M.; van der Poll, T. S.; Henson, Z. B.; Nguyen, T. Q.; Bazan, G. C. *Adv. Mater.* **2013**, *25*, 4403−4406.

(36) Badgujar, S.; Song, C. E.; Oh, S.; Shin, W. S.; Moon, S.-J.; Lee, J.-C.; Jung, I. H.; Lee, S. K. *J. Mater. Chem. A* **2016**, *4*, 16335−16340.

(37) Kraabel, B.; Lee, C. H.; McBranch, D.; Moses, D.; Sariciftci, N. S.; Heeger, A. J. *Chem. Phys. Lett.* **1993**, *213*, 389−394.

(38) Sension, R. J.; Szarka, A. Z.; Smith, G. R.; Hochstrasser, R. M. *Chem. Phys. Lett.* **1991**, *185*, 179−183.

(39) Sariciftci, N. S.; Hebger, A. J. *Int. J. Mod. Phys. B* **1994**, *8*, 237−274.

(40) Zhang, R.; Yang, H.; Zhou, K.; Zhang, J. D.; Yu, X. H.; Liu, J. G.; Han, Y. C. *Macromolecules* **2016**, *49*, 6987−6996.

(41) Zhan, C. L.; Yao, J. N. *Chem. Mater.* **2016**, *28*, 1948−1964.

(42) Kang, H.; Kim, K.-H.; Choi, J.; Lee, C.; Kim, B. J. *ACS Macro Lett.* **2014**, *3*, 1009−1014.

(43) Zimmerman, J. D.; Xiao, X.; Renshaw, C. K.; Wang, S. Y.; Diev, V. V.; Thompson, M. E.; Forrest, S. R. *Nano Lett.* **2012**, *12*, 4366−4371.

(44) Wessendorf, C. D.; Schulz, G. L.; Mishra, A.; Kar, P.; Ata, I.; Weidelener, M.; Urdanpilleta, M.; Hanisch, J.; Mena-Osteritz, E.; Linden, M.; Ahlswede, E.; Bauerle, P. *Adv. Energy Mater.* **2014**, *4*, 1400266.

(45) Wang, J. L.; Xiao, F.; Yan, J.; Wu, Z.; Liu, K. K.; Chang, Z. F.; Zhang, R. B.; Chen, H.; Wu, H. B.; Cao, Y. *Adv. Funct. Mater.* **2016**, *26*, 1803−1812.

(46) Schulz, G. L.; Lobert, M.; Ata, I.; Urdanpilleta, M.; Linden, M.; Mishra, A.; Bauerle, P. *J. Mater. Chem. A* **2015**, *3*, 13738−13748.

(47) Zhang, R.; Yang, H.; Zhou, K.; Zhang, J.; Yu, X.; Liu, J.; Han, Y. *Macromolecules* **2016**, *49*, 6987−6996.

(48) Ye, L.; Jiao, X. C.; Zhou, M.; Zhang, S. Q.; Yao, H. F.; Zhao, W. C.; Xia, A. D.; Ade, H.; Hou, J. H. *Adv. Mater.* **2015**, *27*, 6046−6054.

(49) Ye, L.; Jiao, X. C.; Zhang, H.; Li, S. S.; Yao, H. F.; Ade, H.; Hou, J. H. *Macromolecules* **2015**, *48*, 7156−7163.

(50) Chen, Y. S.; Wan, X. J.; Long, G. K. *Acc. Chem. Res.* **2013**, *46*, 2645−2655.

(51) Lin, Y. Z.; Wang, J. Y.; Zhang, Z. G.; Bai, H. T.; Li, Y. F.; Zhu, D. B.; Zhan, X. W. *Adv. Mater.* **2015**, *27*, 1170−1174.

(52) Yao, H.; Chen, Y.; Qin, Y.; Yu, R.; Cui, Y.; Yang, B.; Li, S.; Zhang, K.; Hou, J. *Adv. Mater.* **2016**, *28*, 8283−8287.

(53) Li, Y. F. *Acc. Chem. Res.* **2012**, *45*, 723−733.

(54) Yao, H. F.; Ye, L.; Zhang, H.; Li, S. S.; Zhang, S. Q.; Hou, J. H. *Chem. Rev.* **2016**, *116*, 7397−7457.

(55) Ye, L.; Zhang, S. Q.; Huo, L. J.; Zhang, M. J.; Hou, J. H. *Acc. Chem. Res.* **2014**, *47*, 1595−1603.

(56) Lin, Y. Z.; He, Q.; Zhao, F. W.; Huo, L. J.; Mai, J. Q.; Lu, X. H.; Su, C. J.; Li, T. F.; Wang, J. Y.; Zhu, J. S.; Sun, Y. M.; Wang, C. R.; Zhan, X. W. *J. Am. Chem. Soc.* **2016**, *138*, 2973−2976.

(57) Zhou, J. Y.; Wan, X. J.; Liu, Y. S.; Zuo, Y.; Li, Z.; He, G. R.; Long, G. K.; Ni, W.; Li, C. X.; Su, X. C.; Chen, Y. S. *J. Am. Chem. Soc.* **2012**, *134*, 16345−16351.

(58) Zhou, J. Y.; Zuo, Y.; Wan, X. J.; Long, G. K.; Zhang, Q.; Ni, W.; Liu, Y. S.; Li, Z.; He, G. R.; Li, C. X.; Kan, B.; Li, M. M.; Chen, Y. S. *J. Am. Chem. Soc.* **2013**, *135*, 8484−8487.

(59) Bakulin, A. A.; Rao, A.; Pavelyev, V. G.; van Loosdrecht, P. H. M.; Pshenichnikov, M. S.; Niedzialek, D.; Cornil, J.; Beljonne, D.; Friend, R. H. *Science* **2012**, *335*, 1340−1344.

(60) Menke, S. M.; Holmes, R. J. *Energy Environ. Sci.* **2014**, *7*, 499−512.

(61) Blom, P. W. M.; de Jong, M. J. M.; Vleggaar, J. J. M. *Appl. Phys. Lett.* **1996**, *68*, 3308−3310.

(62) Mihailetchi, V. D.; Koster, L. J. A.; Hummelen, J. C.; Blom, P. W. M. *Phys. Rev. Lett.* **2004**, *93*, 216601.

(63) Kyaw, A. K. K.; Wang, D. H.; Wynands, D.; Zhang, J.; Nguyen, T. Q.; Bazan, G. C.; Heeger, A. J. *Nano Lett.* **2013**, *13*, 3796−3801.

(64) Lenes, M.; Morana, M.; Brabec, C. J.; Blom, P. W. M. *Adv. Funct. Mater.* **2009**, *19*, 1106−1111.

(65) Müller-Buschbaum, P. *Adv. Mater.* **2014**, *26*, 7692−7709.

(66) Lilliu, S.; Agostinelli, T.; Pires, E.; Hampton, M.; Nelson, J.; Macdonald, J. E. *Macromolecules* **2011**, *44*, 2725−2734.

(67) Ruderer, M. A.; Guo, S.; Meier, R.; Chiang, H.-Y.; Körstgens, V.; Wiedersich, J.; Perlich, J.; Roth, S. V.; Müller-Buschbaum, P. *Adv. Funct. Mater.* **2011**, *21*, 3382−3391.